Structure and electronic properties of domain walls and stacking fault defects in prospective photoferroic materials bournonite and enargite ⓕ

ⓘ O. M. Rigby, ⓘ T. Richards-Hlabangana, ⓘ Q. M. Ramasse, et al.

COLLECTIONS

ⓕ This paper was selected as Featured

View Online   Export Citation   CrossMark

ARTICLES YOU MAY BE INTERESTED IN

Radiation effects in ultra-thin GaAs solar cells
Journal of Applied Physics **132**, 184501 (2022); https://doi.org/10.1063/5.0103381

Optically thick GaInAs/GaAsP strain-balanced quantum-well tandem solar cells with 29.2% efficiency under the AM0 space spectrum
Journal of Applied Physics **132**, 184502 (2022); https://doi.org/10.1063/5.0125998

A comparative study of finite element schemes for micromagnetic mechanically coupled simulations
Journal of Applied Physics **132**, 183903 (2022); https://doi.org/10.1063/5.0105613

AIP Publishing

Structure and electronic properties of domain walls and stacking fault defects in prospective photoferroic materials bournonite and enargite

O. M. Rigby,[1,a] T. Richards-Hlabangana,[2] Q. M. Ramasse,[3,4,5] I. MacLaren,[6] R. A. Lomas-Zapata,[1] M. S. Rumsey,[7] K. P. McKenna,[2] and B. G. Mendis[1]

AFFILIATIONS

[1]Department of Physics, Durham University, South Road, Durham DH1 3LE, United Kingdom
[2]Department of Physics, University of York, Heslington, York YO10 5DD, United Kingdom
[3]SuperSTEM, SciTech Daresbury Campus, Daresbury WA4 4AD, United Kingdom
[4]School of Physics and Astronomy, University of Leeds, Leeds LS2 9TJ, United Kingdom
[5]School of Chemical and Process Engineering, University of Leeds, Leeds LS2 9TJ, United Kingdom
[6]School of Physics and Astronomy, University of Glasgow, Glasgow G12 8QQ, United Kingdom
[7]Mineral and Planetary Science Division, Earth Sciences Department, Natural History Museum, Cromwell Road, London SW7 5BD, United Kingdom

[a]Author to whom correspondence should be addressed: oliver.rigby@durham.ac.uk

ABSTRACT

Bournonite ($CuPbSbS_3$) and enargite (Cu_3AsS_4) have recently been used as absorber layers in thin-film photovoltaic devices due to their ideal bandgap and ferroelectric properties. An understanding of the ferroelectric domain structure in these materials is required so that the benefits of the internal depolarizing electric fields can be fully exploited. Here, the atomic structure and electronic properties of domain walls (DWs) are elucidated through a combined aberration-corrected scanning transmission electron microscopy and density functional theory study. ∼90° and 180° DWs are observed in bournonite. As the 180° DW is charge neutral, it cannot contribute to the anomalous photovoltaic effect that leads to high open circuit voltages. The ∼90° DW shows a slight offset across the boundary, but the contributions of this to the anomalous photovoltaic effect are negligible. The DWs are also electrically passive, i.e., they do not result in significant recombination and do not block charge carrier transport. A high density of stacking faults (SF) was, however, observed in enargite. The SFs have a large number of defect states within the bandgap, which would lower the device efficiency through Shockley–Read–Hall recombination.

I. INTRODUCTION

Ferroelectrics are a subset of pyroelectric materials that exhibit a net electric dipole moment in the unit cell and, hence, a spontaneous polarization.[1] This means ferroelectric materials have a non-centrosymmetric unit cell, limiting the number of possible crystallographic point groups to 10 out of the 32 available.[2] In addition to this, the polarization is reversible under an applied electric field and becomes zero above a certain temperature (the Curie temperature, T_C). The use of ferroelectric materials as absorber layers in thin-film p–n junction photovoltaics (PV) is a relatively new concept and, among other factors, is motivated by the presence of an additional internal electric field for charge separation.

The internal electric field is due to a discontinuity in polarization, such as at a free surface, interface, or domain wall (DW) boundary. Apart from charge separation, the internal field can also modify the Schottky energy barrier at metal-ferroelectric semiconductor interfaces,[3,4] thus potentially enhancing charge extraction

from the device, as well as enable photocurrent switching when an electric field above the coercive field is applied.[5]

A further unique property of photo-ferroelectric, or "photoferroic," materials is the observation of an above bandgap open circuit voltage (Voc), sometimes greater than 10 V.[6] In the literature, this is referred to as the anomalous photovoltaic effect (APV). In a conventional semiconductor, V_{oc} is limited by the bandgap, but for the APV effect, V_{oc} is linearly dependent on electrode spacing.[3,7] Several mechanisms have been proposed to explain the APV effect, such as a built-in asymmetry in scattering and absorption centers for a non-centrosymmetric crystal.[4,8] Measurements on epitaxial BiFeO₃ (BFO) metal-ferroelectric-metal (MFM) devices suggested that DWs may be responsible for the APV effect.[6] It was proposed that the strong internal electric field at the DW separated photogenerated electrons and holes before they could recombine, thereby generating a 10 mV photovoltage across the DW.[6,9] Series addition of the photovoltage across parallel DWs can, therefore, lead to unusually high values for the V_{oc}. Although the DW mechanism for APV is debated,[7] the prospect of large V_{oc} values for photoferroics could potentially reverse the trend of relatively large V_{oc} deficits observed in traditional thin-film PV materials, such as CdTe,[10] Cu(In,Ga)(S,Se)₂,[11] and Cu₂ZnSn(S,Se)₄,[12] which is currently limiting the achievement of high-efficiency devices.

Early photoferroic material devices include BaTiO₃ (BTO) and BFO, but these still do not show commercially viable efficiencies.[4] This is mainly due to bandgaps that exceeded the ideal Shockley–Queisser value (on the order of 3.2 eV for BTO[13] and 2.5 eV for BFO[14]) and intrinsically low bulk conductivities for efficient photoconversion. It is, therefore, worth investigating other polar materials that have a more optimal bandgap. Inspired by naturally occurring minerals, Wallace et al.[15] highlighted two candidate ferroelectric materials, bournonite (CuPbSbS₃) and enargite (Cu₃AsS₄), which have optical properties suitable for PV applications. To our knowledge, the polarization switching by an electric field has not been experimentally demonstrated in either bournonite or enargite, but we shall nevertheless still refer to these materials as being ferroelectric, consistent with the terminology used in Ref. 15. Bournonite and enargite are of space group Pmn2₁, with orthorhombic unit cells and have direct bandgaps of ~1.3[16] and 1.4 eV, respectively [see Figs. 1(a) and 4(a) for corresponding unit cell structures]. The ferroelectric nature of both of these materials originates from the relative ion positions of their respective unit cells. Wallace et al. calculated spontaneous polarization values of $1.83\,\mu C\,cm^{-2}$ for bournonite and $67.8\,\mu C\,cm^{-2}$ for enargite.[15] Recent work on bournonite and enargite has focused on the synthesis[16–20] and the electronic structure.[21–27] The first solar cell using a bournonite absorber layer was made by Tang and co-workers in 2020 with a champion efficiency of 2.23%,[28] which their group has since increased through improved crystallinity to 2.6%.[29] The first enargite solar cell was made by McClary et al., and while its performance was poor at 0.18%, there are promising results regarding its photogenerated carrier lifetime (~1.4 ns).[20,30] Using density functional theory simulations, Liu et al. also showed that the point defects with lowest formation energies in bournonite are all shallow states, suggesting that the material is defect tolerant as far as point defects are concerned.[28]

To our knowledge, there has been no study on possible DWs in bournonite or enargite. Theoretically, the permissible DW planes can be deduced by knowledge of the paraelectric phase and polarization direction using the criterion of mechanical compatibility, i.e. there should be no residual mechanical stress across the
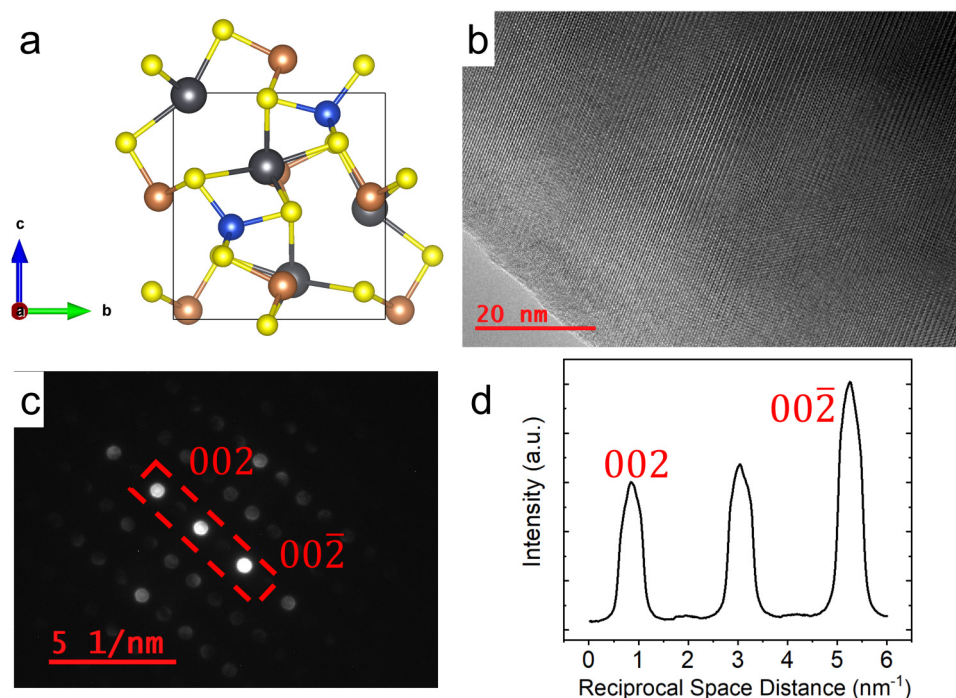

FIG. 1. (a) Unit cell of bournonite projected along the [100] axis with Pb: gray, Cu: blue, Sb: brown, and S: yellow. (b) HREM image of defect-free bournonite in the [110] orientation, and (c) the corresponding CBED pattern. (d) Intensity profile extracted from the red dashed box region in (c) with Bragg reflections labeled.

DW boundary.[31] However, taking bournonite as an example, the Curie temperature is unknown and thermogravimetric data[28] indicate that the material decomposes before any potential transition to a paraelectric phase. Furthermore, bulk samples quenched from 673 K to room temperature indicate no change in the crystal structure.[32] Therefore, the nature of ferroelectric domains must be experimentally characterized for these materials. The domain configuration is fundamental to device performance, since it governs charge separation, charge extraction through electrical contacts, photocurrent switching, and (potentially) APV effects.

In this paper, we use aberration-corrected scanning transmission electron microscopy (STEM) to characterize the atomic structure of ferroelectric DWs and other planar defects, notably stacking faults, observed in bulk samples of bournonite and enargite. Density functional theory (DFT) simulations are used to calculate the bandgap states at planar defects, thus enabling a qualitative assessment of the impact of defects on Shockley–Read–Hall (SRH) recombination. The APV and SRH recombination have opposing effects on the V_{oc}. A detailed structural and electronic characterization of the domain structure is important for designing solar cells that utilize ferroelectricity to improve efficiencies beyond standard thin-film semiconductor devices.

II. EXPERIMENTAL DETAILS

Mineral samples of bournonite (Rio Tinto Mine, Andalucia, Spain) and enargite (Butte, Montana, USA) were acquired from the Natural History Museum collection in London. X-ray diffraction (XRD) plots for these minerals can be found in Fig. S1 in the supplementary material and are in agreement with the reference spectra for bournonite and enargite, indicating largely phase pure material. Transmission electron microscopy (TEM) samples were prepared by crushing the material in a mortar and pestle before dispersing in isopropyl alcohol and depositing on a holey carbon grid. A JEOL 2100F field emission gun TEM, operating at 200 kV, was used to check the chemical purity of the sample using energy-dispersive x-ray (EDX) analysis. This microscope was also used for convergent beam electron diffraction (CBED) measurements of the sample polarity. Aberration-corrected STEM imaging of the bournonite sample was carried out using the University of Glasgow JEOL ARM 200CF microscope operating at 200 kV, while the enargite sample was imaged at 60 kV using the Nion "Hermes" microscope at the SuperSTEM facility in Daresbury.

Spin-polarized DFT calculations were carried out using the projector-augmented wave method as implemented in the Vienna *Ab initio* Simulation Package (VASP).[33,34] For enargite, the following electrons were treated as valence electrons: Cu (3p, 3d, 4s), As (4s, 4p), and S (3s, 3p), and for bournonite: Cu (3p, 3d, 4s), Sb (5s, 5p), Pb (5d, 6s, 6p), and S (3s, 3p). The bulk unit cell of bournonite was optimized using the Perdew–Burke–Ernzerhof (PBE) exchange-correlation functional with a $3 \times 3 \times 3$ gamma centered k-point grid for Brillouin zone sampling, a 520 eV plane wave cutoff, and a force tolerance for geometry optimization of 0.01 eV Å^{-1}. The optimized lattice constants of bournonite were obtained as a = 7.851 Å, b = 8.292 Å, and c = 9.018 Å, in reasonable agreement with experiment (within 4%). The bulk unit cell of enargite was optimized using the HSE06 hybrid functional[35] with a

$4 \times 4 \times 4$ gamma centered k-point grid for Brillouin zone sampling, a 520 eV plane wave cutoff, and a force tolerance for geometry optimization of 0.01 eV Å^{-1}. The optimized lattice constants of enargite were obtained as a = 7.398 Å, b = 6.432 Å, and c = 6.141 Å, in excellent agreement with experiment (within 0.3%). Structures and band-projected electron densities were visualized using the VESTA package.[36]

Supercells for modelling extended defects were constructed from the optimized bulk structures using our freely available GBMaker code.[37] The approach follows that described in our previous studies of extended defects in a wide range of materials including MgO,[38,39] TiO$_2$,[40] HfO$_2$,[41] TiN,[42] Sb$_2$Se$_3$,[43] and lead halide perovskites.[44] For bournonite, domain wall defects were created on (010) and (011) planes for 180° and near 90° domain walls, respectively. For enargite, various supercells corresponding to different stacking faults on the (001) plane were constructed. All prospective defect models were fully optimized with respect to the position of all atoms and the supercell dimension in the direction perpendicular to the extended defect. The k-point grids were reduced to $3 \times 3 \times 1$ and $4 \times 4 \times 1$ for bournonite and enargite, respectively. The stability of the extended defects is quantified by evaluating the formation energies,

$$E_f = \frac{E_{ED} - E_{Bulk}}{2A},$$

where E_{ED} is the total energy of the supercell containing the extended defect, E_{Bulk} is the total energy of the same number of formula units of perfect bulk crystal, and A is the cross sectional area of each of the extended defects in the supercell. Formation energies were calculated with respect to a bulk supercell of comparable dimensions to the extended defect supercell (to minimize errors associated with comparing the energy of supercells of different sizes). To accurately model the electronic properties of the most stable optimized structures, the HSE06 hybrid functional was used (without further geometry optimization for bournonite).

III. RESULTS AND DISCUSSION

A. Bournonite

DFT simulations (see supplementary information in Ref. 15) have shown that polarization in bournonite is along the c-axis, which is also a 2$_1$ screw axis. The polarity of a crystal can be determined using the CBED technique,[45] which has previously been applied to ferroelectrics, such as BTO.[46] The method relies on detecting intensity asymmetries in Friedel pairs (i.e., hkl and $\overline{hkl}$ reflections) due to dynamical electron diffraction. Tanaka *et al.*[47] have classified the suitable crystal orientations for the CBED analysis of polarity; for the Pmn2$_1$ space group of bournonite and enargite, the required crystal orientations have Miller indices of the form $\langle uv0 \rangle$. Figure 1(b) shows a high-resolution electron microscopy (HREM) image of bournonite oriented along [$\overline{1}$10]. The imaged region is free from any crystal defects. A CBED pattern was acquired from this region and is shown in Fig. 1(c). The 001 and 00$\overline{1}$ reflections are weak due to the extinction rules for a 2$_1$ screw axis.[48] Furthermore, the intensities of the 002/00$\overline{2}$ Friedel pair is asymmetric, as indicated in the intensity profile plot of Fig. 1(d).
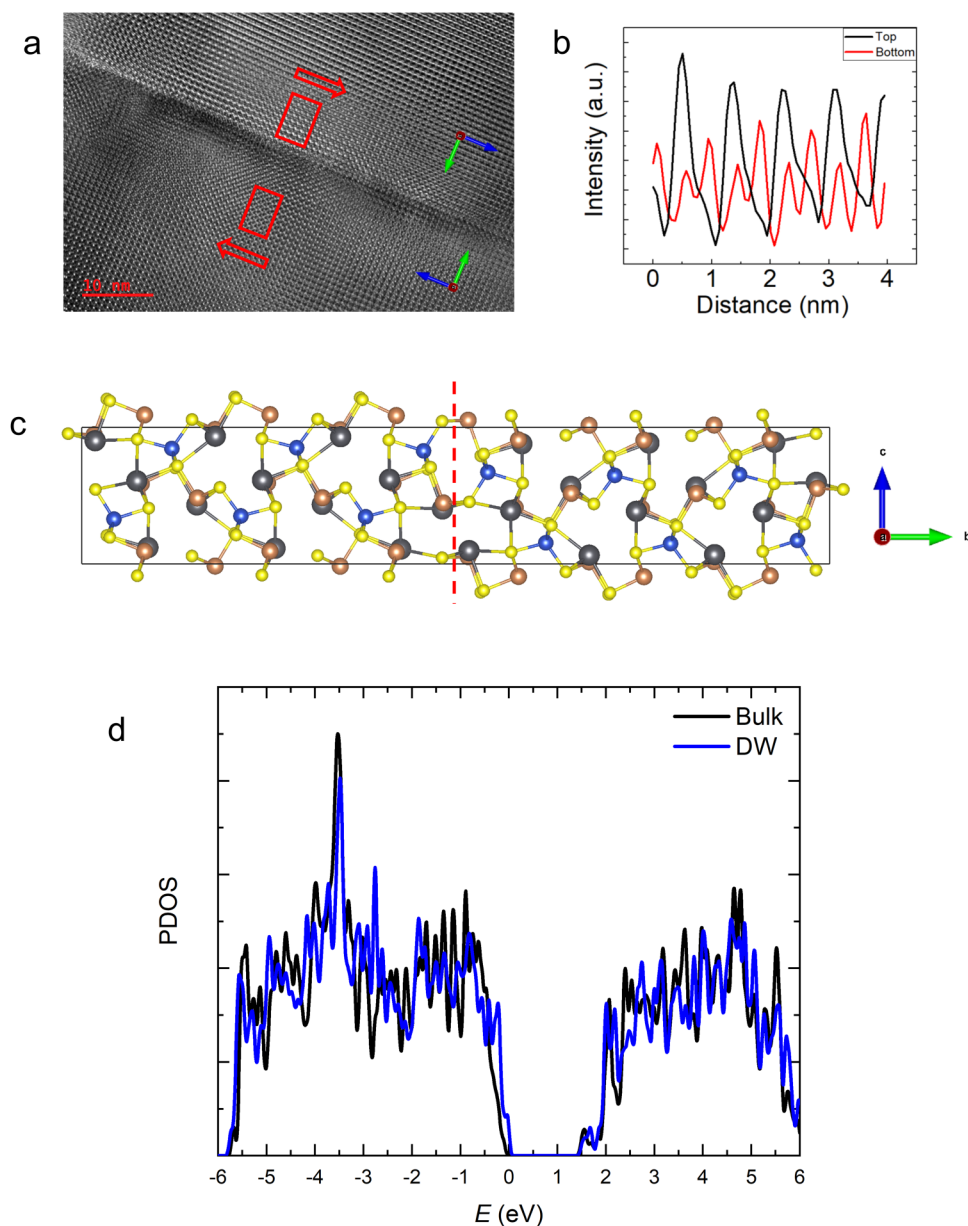
FIG. 2. (a) HREM image of [100]-oriented bournonite with a 180° DW plane along (010). Red arrows show orientation of the polarization vector on either side of the DW. The domains extend to the edges of the particle and are tens of nanometers across. (b) HREM intensity profile along $\langle 001 \rangle$ extracted from the box regions in (a) from above the DW (top) and below the DW (bottom). The profiles show alternating peaks. (c) DFT model of the 180° DW, with the red dashed line showing the DW plane in the middle of the supercell (Pb: gray, Cu: blue, Sb: brown, and S: yellow). (d) Local DOS of bulk bournonite and 180° DW regions. The VBM in the bulk is arbitrarily assigned as zero energy level.

Strictly speaking, Friedel pairs that do not correspond to the polarization direction can also show CBED intensity asymmetries.[45,47] Our results are, therefore, consistent with the polar nature of bournonite, but is not a rigorous verification of its polarization direction.

The polar nature of bournonite suggests the formation of domains, and indeed several DWs were observed. Figure 2(a) shows an HREM image of [100]-oriented bournonite, with a (010) planar defect that also contains the $\langle 001 \rangle$ polarization vector. A fast Fourier transform (FFT) of the image did not reveal any "extra"

reflections, indicating that coherency is maintained across the planar defect. The HREM lattice fringe intensity along the $\langle 001 \rangle$ direction was extracted from box regions on either side of the defect, as shown in Fig. 2(a). The extracted intensity is integrated in a direction normal to the planar defect, and the resulting line profiles for top and bottom crystal regions are plotted in Fig. 2(b).

The profiles consist of periodically repeating pairs of peaks with high and low intensities (for the top profile, the low-intensity peak appears as a "shoulder"). The distance between high-intensity peaks, i.e., the periodic repeat distance, is 8.84 ± 0.09 Å, as measured using Gaussian curve fitting, which is similar to the 8.7 Å c-axis lattice parameter. The high and low intensity peak pair separation for the bottom crystal is 4.42 ± 0.05 Å, i.e., half the measured periodic repeat distance. As discussed previously, the 001 reflections are kinematically forbidden in bournonite due to the 2_1 symmetry axis. This would result in different intensities for (002) and (001) crystal planes in HREM and is likely to be the origin of the high- and low-intensity peak pairs observed in the image. Comparing the profiles in Fig. 2(b), it is clear that there is a switching in the peak pair orientation.

This suggests that the planar defect could be either a SF with a c/2 shear on the (010) plane or, alternatively, a 180° DW with a reversal in the polarization direction on either side of the defect boundary. The former is unlikely due to the relatively large shear vector ($\sim$4.4 Å), as well as the reduced symmetry of orthorhombic bournonite, which may result in a large number of wrong bonds. Switching the polarization direction will reverse the asymmetry of the $002/00\bar{2}$ Friedel pair intensity [Fig. 1(c)], which can be shown to give rise to a HREM contrast reversal (see supplementary material). As polarization is oriented parallel to the 180° DW, there is no change in the polarization component normal to the defect, and hence, the DW is "uncharged."

The absence of bound charge at the 180° DW means that no local electric field is generated, and therefore, these DWs are not expected to contribute to the APV effect.[6] However, DWs may also create defect energy states within the bandgap, thereby reducing the photovoltage through SRH recombination. To investigate this further, the electronic structure of the DW was simulated using DFT. Unfortunately, aberration-corrected STEM images of the 180° DW are not available, and therefore, no data exists for the DW atomic structure, particularly its termination layer. In order to preserve periodic boundary conditions, a supercell was created with two equivalent 180° DWs in the middle and at the ends along the b-axis [Fig. 2(c)]. The simulated DW terminates at the Pb/Sb cation planes, as shown by the red dashed line in Fig. 2(c). The formation energy of the DW following full geometry optimization was low ($E_f = 0.10$ J m^{-2}), confirming that the termination considered is reasonable. Furthermore, the analysis of atomic displacements following supercell relaxation showed that the DW width was $\sim$20 Å, with the largest displacement no more than 0.5 Å (see Fig. S2 in the supplementary material). The local density of states (DOS) for the DW region and bulk bournonite are shown superimposed in Fig. 2(d). No bandgap states are observed at the DW, which is consistent with the high degree of lattice coherency observed in Fig. 2(a). Furthermore, there is no energy misalignment of the valence band maximum (VBM) or conduction band minimum (CBM) between the DW plane and the perfect crystal region. Hence, there is no energy barrier to electron or hole transport

across the DW; this should be compared to DWs in BFO, which have higher conductivity than the perfect crystal,[49] or grain boundaries in CuInSe$_2$, where valence band misalignment causes the grain boundary to act as a hole barrier.[50] Figure 3(a) shows an annular dark field (ADF) image of [100]-oriented bournonite acquired using an aberration-corrected STEM. The ADF detector inner angle is sufficiently large to give atomic number contrast, such that heavy atoms have higher intensity in the image. For [100]-bournonite, the Pb/Sb columns, therefore, appear bright, while the Cu containing columns have much weaker intensity, and the S columns are below the signal-to-noise. In Fig. 3(a), a faint vertical band of higher intensity contrast, spanning several atoms in width, is observed. This suggests the presence of a planar defect, with the higher contrast potentially due to strain associated with the defect (see below). The FFT acquired from the box region containing the planar defect is shown in Fig. 3(b). The Bragg reflections appear in pairs, one example of which is highlighted. FFT patterns acquired from either side of the planar defect were indexed as being along the [100]-orientation. However, the b and c-axes were reversed between the two regions, indicating a rotation of the crystal axes on crossing the planar defect. This implies that the planar defect is a $\sim$90° DW, and the Bragg reflection pairs are due to the different values for b and c-lattice parameters (8.15 and 8.70 Å, respectively).[51] Several other $\sim$90° DWs were found (as seen in Fig. S3 in the supplementary material), which also reversed the b and c-axes between domains. For a 90° rigid body rotation, a given set of Bragg reflection pairs in the FFT must lie along a straight line passing through the unscattered beam. This is, however, not observed in Fig. 3(b), and the relative positions of Bragg reflection pairs are more consistent with a 87° rotation.

The atomic resolution detail in Fig. 3(a) enables a model structure of a near 90° DW to be constructed for DFT modelling. We consider an extended defect forming on a (011) plane with crystal polarization mirrored on either side of the defect. Due to the slight mismatch between b and c lattice parameters, this corresponds to a 85.2° domain wall, close to the experimentally observed value. The ADF-STEM image of the DW clearly shows that Pb–Sb layers from each grain meet at the DW forming a chevron pattern when viewed along the [100] direction (seen more clearly in Fig. S4 in the supplementary material). This observation constrains the possible intergrain translation vectors. Six different prospective DW supercells were constructed, consistent with the observed chevron pattern, and fully optimized. The most stable geometry optimized DFT supercell ($E_f = 7$ m J m^{-2}) is shown in Fig. 3(c) and overlayed with the ADF image in Fig. 3(d). There is good agreement with the experimental image, indicating that many of the essential features have been correctly reproduced in the model. The local DOS for the bulk and DW regions are shown superimposed in Fig. 3(e). No bandgap defect states are observed at the DW, and therefore, any SRH recombination is expected to be low. The energy alignment of the VBM and CBM also indicate that the DW does not impede electron or hole charge transport. Furthermore, the DW is not fully charge neutral due to the small offset from perfect 90° misorientation. However, due to the small nature of the offset, any charge build-up will be negligible. In contrast, the DW APV effect reported in Yang *et al.*[6] had 71° DWs where there is a much larger change in polarization component normal to the DW. The optoelectronic properties of the $\sim$90° DW are, therefore, very similar to
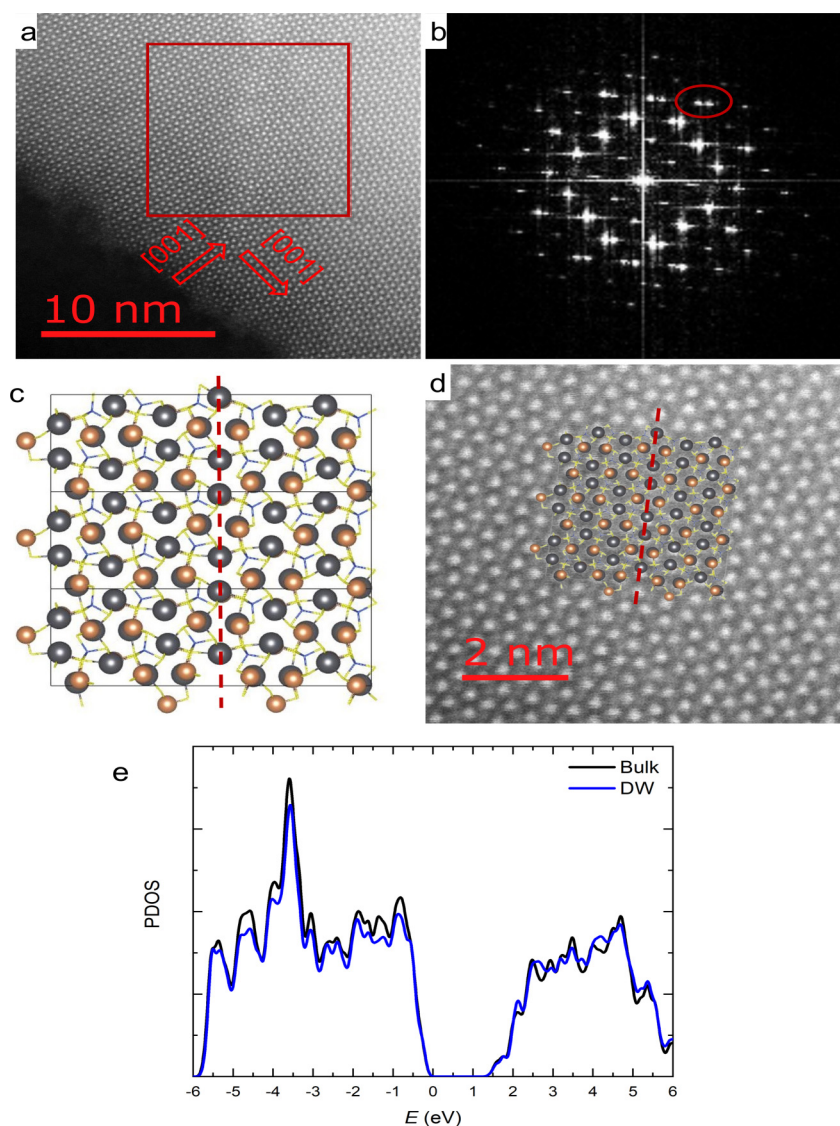
FIG. 3. (a) ADF image of a ∼90° DW in [100]-oriented bournonite. Red arrows show the orientation of the polarization vector on either side of the DW. (b) FFT of the region indicated by the red square in (a). Many of the Bragg reflections appear in pairs, an example of which is highlighted. (c) Geometry optimized DFT model for ∼90° DW (Pb: grey, Cu: blue, Sb: brown and S: yellow), which is over-layed with the experimental image in (d). The red dashed line indicates the DW plane. (e) The calculated local DOS for the bulk and ∼90° DW (the VBM of the bulk region is arbitrarily assigned zero energy).

the 180° DW. Characterization of multiple grains did not reveal any other DW types, which suggests that ∼90° and 180° DWs are the lowest energy DWs in bournonite.

B. Enargite

For enargite, also of space group $Pmn2_1$, the polarization is expected along the c-axis as well (see supplementary information in Ref. 6) Although enargite is orthorhombic, its crystal structure has many similarities with the hexagonal, wurtzite unit cell.[52] This is evident from the [100] projection of enargite, where the (001) planes follow the AB stacking sequence of the hexagonal basal planes in wurtzite [Fig. 4(a)]. To confirm the polar nature of enargite, CBED patterns were acquired from a defect-free region along the [100]

zone axis [Fig. 4(b)]. Similar to bournonite, the 002/00$\bar{2}$ Friedel pair reflections show an intensity asymmetry [Figs. 4(c) and 4(d)], as required for a non-centrosymmetric crystal structure. Unlike bournonite however, many of the enargite grains showed high-density planar defects. An example is shown in Fig. 5(a), which is an HREM image of [2$\bar{1}$0] oriented enargite with several end-on planar defects parallel to (001) planes. To confirm the nature of these defects, CBED patterns were acquired from either side of the defect, as shown in Figs. 5(b)–5(e). Since there is no reversal in the 002/00$\bar{2}$ Friedel pair intensity asymmetry, the polarity does not change on crossing the planar defect. Therefore, the planar defects cannot be DWs, but some other defect type, such as stacking faults (SF).

Stacking faults and regions with cubic stacking sequence have previously been reported in enargite.[52] No polarity inversion was
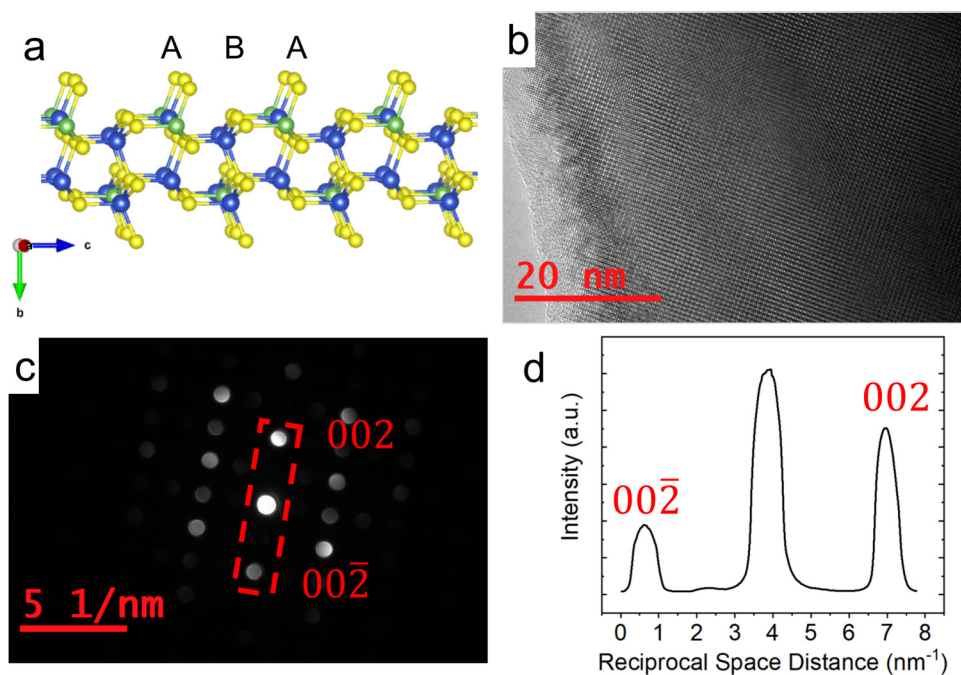
FIG. 4. (a) Enargite viewed close to [100] projection, with S: yellow, Cu: blue, and mixed columns of Cu and As in green. The crystal has an AB stacking sequence along the c-axis (b). HREM image of a defect-free region of enargite in the [100]-orientation and (c) the corresponding CBED pattern. (d) Intensity profile extracted from the red dashed box region in (c) with Bragg reflections labeled.

observed on either side of the defect regions,[52] consistent with our results. To determine the SF atomic structure, aberration-corrected STEM ADF imaging was performed on [100]-oriented enargite. Figure 6(a) shows a single SF in the field of view. The ADF image consists of "dumbbells," where each dumbbell corresponds to two closely spaced atom columns. Comparing with Fig. 5(a), each dumbbell consists of a column of either pure Cu or mixed Cu/As bonded to S.
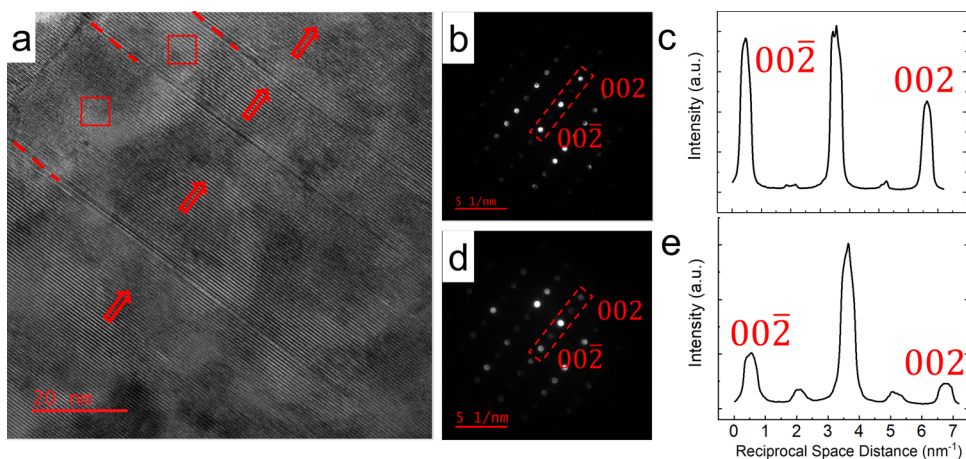

FIG. 5. (a) HREM image of [2$\bar{1}$0] oriented enargite showing several SFs (dashed lines indicate the SFs, red arrows show the direction of polarity). CBED patterns were acquired from the top and bottom box regions positioned on either side of a single SF and are shown in (b) and (d), respectively. The intensity profiles acquired along the dashed boxes in (b) and (d) are shown in (c) and (e), respectively.

In the bulk regions, away from the SF, the dumbbells are oriented in a chevron pattern, signifying the AB stacking sequence along the c-axis. At the SF, however, the stacking sequence is ABBA. This shear could originate from dumbbell pairs of same type matching (i.e., Cu to Cu dumbbells or Cu/As to Cu/As dumbbells), which would result in similar intensities on either side of the SF. Instead, it is seen in the inset to Fig. 6(b) that doublet peaks on either side of the SF correlate to columns of mixed Cu/As dumbbells (high intensity) and columns of pure Cu dumbbells (low intensity). This sequence can be generated by removing a B layer and shearing the top half of the crystal by a $\frac{1}{3}[010]$ vector [Fig. 6(c)]. This process is similar to generating a low-energy intrinsic SF in hexagonal crystals, where a basal plane is removed and the top half of the crystal is sheared by a non-lattice translation vector.[53] Similar to hexagonal crystals, the SF in enargite also preserves the nearest neighbor cations.

For enargite, various supercells corresponding to different stacking faults on the (001) plane were constructed. The two most stable were the ABBA stacking fault observed experimentally ($E_f = 0.43$ Jm^{-2}) and an ABAB stacking fault with in-plane translation of $\frac{1}{2}b$ ($E_f = 0.44$ Jm^{-2}). We note that while these formation energies may appear high compared to SFs in some metals, they are low compared to grain boundaries and twins in non-metallic compounds. The relatively low energy is likely a result of preserving the nearest neighbor cations across the SF. Figure 6(d) shows the local DOS calculated for the SF and bulk region of enargite. The latter was calculated for supercell regions further away from the SF. Defect states are observed in the DOS that reduce the bandgap near the SF. These states are associated with interfacial ions and have primarily Cu 3d and S 3p character (see Fig. S5 in the supplementary material). The hole states near the VBM are shallow, but the deep electron states 0.2 eV below the CBM could significantly affect recombination of photogenerated charge carriers. This is undesirable, especially since the enargite was found to contain a high density of SF defects. Our TEM results did not
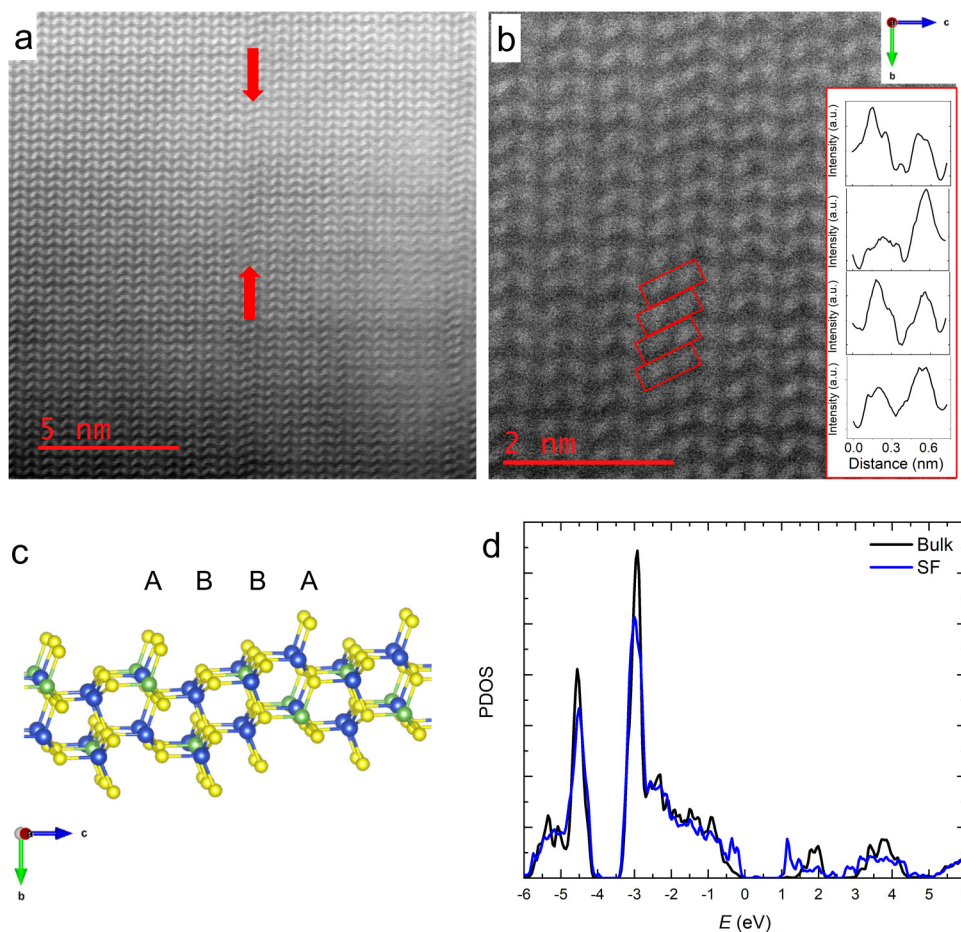

FIG. 6. (a) ADF image of [100]-enargite showing a single SF along a (001) plane (arrowed). (b) Enlarged view of the SF with inset intensity profiles taken across the SF at locations of red boxes. (c) SF model tilted to show Cu/As and pure Cu columns, viewed close to [100] projection. (d) Local DOS of the SF and a bulk region not containing an SF in enargite.

find any evidence of DWs in enargite, although their presence cannot be ruled out.

IV. CONCLUSIONS

The ferroelectric domain configurations of prospective photoferroic materials bournonite ($CuPbSbS_3$) and enargite (Cu_3AsS_4) were characterized using aberration-corrected STEM. The polar nature of both materials was confirmed using CBED. Both 180° and ~90° DWs were found in bournonite. The former had a high degree of coherency and was uncharged, meaning it cannot contribute to the APV effect. The ~90° DW showed a slight offset along the boundary due to the difference in b and c lattice parameters, and although this would lead to bound charges, any contribution to the APV effect would be negligible. Supercell models of DWs for DFT simulations were constructed using the experimental data as a guide. The calculated DOS for both DWs did not reveal any bandgap defect states, and furthermore, there was no band offset for the VBM and CBM between bulk and DW regions. This indicates that the DWs are not strong SRH recombination sites and do not act as blocking layers to charge carrier transport. Although there is no APV effect, the domain configuration can still play an important role in PV device performance. For example, the internal electric field of a poled ferroelectric can be used to enhance charge separation and modify any Schottky energy barrier at a ferroelectric-metal electrode interface. To maximize the internal electric field, the polarization vector must be oriented along the ferroelectric thin-film thickness direction, so that the material should ideally have a c-axis texture. The orientation of polarization is also important. As an example, for efficient charge separation, the polarization vector must point toward the p–n junction, so that minority carrier, photogenerated electrons within the p-type ferroelectric can drift toward the space charge region. In the presence of a 180° DW, some of the domains would, therefore, enhance charge separation, while others would hinder the process.

For enargite, a high density of SFs was observed on the (001) planes. Although enargite is orthorhombic, its crystal structure can be derived from the hexagonal unit cell. In this scheme, the enargite SFs are equivalent to basal slip. STEM images of the atomic structure suggested removal of a c plane followed by a $\frac{1}{3}[010]$ shear. The DFT-simulated SF energy ($0.43\ \mathrm{Jm}^{-2}$) is moderate, largely due to preserving the nearest neighbor cation configuration. DFT also indicated bandgap defect energy levels, particularly below the conduction band minimum. The high density of SFs is, therefore, likely to lead to significant SRH recombination, thereby lowering the V_{oc} of the PV device. SFs have hindered other promising solar absorbers such as CdTe, where investigations into the source of the SFs altered the synthesis methodology to prevent their formation.[54,55] Identifying these SFs early in the development of enargite solar cells could aid in improved device synthesis.

SUPPLEMENTARY MATERIAL

See the supplementary material for XRD plots of mineral samples of bournonite and enargite, an outline of HREM contrast reversal across a 180° DW, DFT calculated absolute atomic displacements within the supercell for a 180° DW in bournonite, a HREM image of the distribution of ~90° DWs in bournonite, the Pb–Sb layer structure at ~90° DWs in bournonite, and the electron density isosurfaces for enargite stacking faults.

AUTHOR DECLARATIONS

Conflict of Interest

The authors have no conflicts to disclose.

Author Contributions

O. M. Rigby: Formal analysis (equal); Investigation (equal); Resources (equal); Writing – original draft (equal). **T. Richards-Hlabangana:** Formal analysis (equal); Investigation (equal); Writing – review & editing (equal). **Q. M. Ramasse:** Investigation (equal); Resources (equal); Writing – review & editing (equal). **I. MacLaren:** Investigation (equal); Resources (equal); Writing – review & editing (equal). **R. A. Lomas-Zapata:** Formal analysis (equal); Writing – review & editing (equal). **M. S. Rumsey:** Resources (equal); Writing – review & editing (equal). **K. P. McKenna:** Formal analysis (equal); Investigation (equal); Writing – original draft (equal); Resources (equal). **B. G. Mendis:** Formal analysis (equal); Investigation (equal); Writing – original draft (equal); Resources (equal).

DATA AVAILABILITY

The data that support the findings of this study are openly available in the University of York Research database (https://doi.org/10.15124/ed070510-2d98-4720-9087-6b86454bc4f9). The data that support the findings of this study are available from the corresponding author upon reasonable request.

REFERENCES

[1]I. E. Castelli, T. Olsen, and Y. Chen, J. Phys. Energy **2**(1), 011001 (2020).
[2]P. S. Halasyamani and K. R. Poeppelmeier, Chem. Mater. **10**, 2753–2769 (1998).
[3]P. Lopez-Varo, L. Bertoluzzi, J. Bisquert, M. Alexe, M. Coll, J. Huang, J. A. Jimenez-Tejada, T. Kirchartz, R. Nechache, F. Rosei, and Y. Yuan, "Physical aspects of ferroelectric semiconductors for photovoltaic solar energy conversion," Phys. Rep. **653**, 1–40 (2016).
[4]C. Paillard, X. Bai, I. Infante, M. Guennou, G. Geneste, M. Alexe, J. Kreisel, and B. Dkhil, Adv. Mater. **28**, 5153–5168 (2016).

[5]D. Lee, S. H. Baek, T. H. Kim, J.-G. Yoon, C. M. Folkman, C. B. Eom, and T. W. Noh, Phys. Rev. B **84**, 125305 (2011).

[6]S. Y. Yang, J. Seidel, S. J. Byrnes, P. Shafer, C. H. Yang, M. D. Rossell, P. Yu, Y. H. Chu, J. F. Scott, J. W. Ager, L. W. Martin, and R. Ramesh, Nat. Nanotechnol. **5**, 143–147 (2010).

[7]A. Bhatnagar, A. Roy Chaudhuri, Y. Heon Kim, D. Hesse, and M. Alexe, Nat. Commun. **4**, 2835 (2013).

[8]K. Butler, J. Frost, and A. Walsh, Energy Environ. Sci. **8**, 838–848 (2015).

[9]J. Seidel, D. Fu, S. Y. Yang, E. Alarcón-Lladó, J. Wu, R. Ramesh, and J. W. Ager, Phys. Rev. Lett. **107**, 126805 (2011).

[10]M. Powalla, S. Paetel, E. Ahlswede, R. Wuerz, C. Wessendorf, and T. Magorian Friedlmeier, Appl. Phys. Rev. **5**, 041602 (2018).

[11]A. Kanevce, K. Ramanathan, and M. Contreras, in *2014 IEEE 40th Photovoltaic Specialist Conference (PVSC)* (IEEE, 2014), pp. 382–386.

[12]S. Bourdais, C. Choné, B. Delatouche, A. Jacob, G. Larramona, C. Moisan, A. Lafond, F. Donatini, G. Rey, S. Siebentritt, A. Walsh, and G. Dennler, Adv. Energy Mater. **6**, 1502276 (2016).

[13]K. Suzuki and K. Kijima, Jpn. J. Appl. Phys. **44**, 2081 (2005).

[14]Y. Jiang, H. Ning, and J. Yu, AIP Adv. **8**, 125334 (2018).

[15]S. K. Wallace, K. L. Svane, W. P. Huhn, T. Zhu, D. B. Mitzi, V. Blum, and A. Walsh, Sustain. Energy Fuels **1**, 1339–1350 (2017).

[16]K. Koskela, B. Melot, and R. Brutchey, J. Am. Chem. Soc. **142**, 6173–6179 (2020).

[17]K. Wei, J. Martin, J. R. Salvador, and G. S. Nolas, Cryst. Growth Des. **15**, 3762–3766 (2015).

[18]Y. T. Alharbi, F. Alam, K. Parvez, M. Missous, and D. J. Lewis, Inorg. Chem. **60**, 13691–13698 (2021).

[19]S. Bairamova, M. Bagieva, S. Agapashaeva, and O. Aliev, Inorg. Mater. **47**, 345–348 (2011).

[20]S. A. McClary, J. Andler, C. A. Handwerker, and R. Agrawal, J. Mater. Chem. C **5**, 6913–6916 (2017).

[21]Y. Dong, A. R. Khabibullin, K. Wei, J. R. Salvador, G. S. Nolas, and L. M. Woods, ChemPhysChem **16**, 3264–3270 (2015).

[22]C. Tablero, Theor. Chem. Acc. **135**, 126 (2016).

[23]S. K. Wallace, K. T. Butler, Y. Hinuma, and A. Walsh, J. Appl. Phys. **125**, 055703 (2019).

[24]S. Kharbish, E. Libowitzky, and A. Beran, Eur. J. Mineral. **21**, 325–333 (2009).

[25]S. Kharbish, G. Giester, and A. Beran, Neues Jahrb Mineral, Abh **187**, 159–166 (2010).

[26]A. Faghaninia, G. D. Yu, U. Aydemir, M. Wood, W. Chen, G. M. Rignanese, G. J. Snyder, G. Hautier, and A. Jain, Phys. Chem. Chem. Phys. **19**, 6743–6756 (2017).

[27]S. McClary, S. Li, X. Yin, P. Dippo, D. Kuciauskas, Y. Yan, J. Baxter, and R. Agrawal, in *Conference Record of the IEEE Photovoltaic Specialists Conference* (IEEE, 2019), pp. 2310–2314.

[28]Y. Liu, B. Yang, M. Zhang, B. Xia, C. Chen, X. Liu, J. Zhong, Z. Xiao, and J. Tang, Nano Energy **71**, 104574 (2020).

[29]M. Zhang, Y. Liu, B. Yang, X. Lin, Y. Lu, J. Zheng, C. Chen, and J. Tang, ACS Appl. Mater. Interfaces **13**, 13273–13280 (2021).

[30]S. McClary, M. Taheri, D. Blach, A. Pradhan, S. Li, L. Huang, J. Baxter, and R. Agrawal, Appl. Phys. Lett. **117**, 162102 (2020).

[31]J. Fousek and V. Janovec, J. Appl. Phys. **40**, 135–142 (1969).

[32]O. M. Aliyev, D. S. Ajdarova, S. T. Bayramova, S. J. Aliyeva, and V. M. Ragimova, Azerbaijan Chem. J. **2**(2), 51–54 (2016).

[33]G. Kresse and J. Furthmüller, Comput. Mater. Sci. **6**, 15–50 (1996).

[34]G. Kresse and J. Furthmüller, Phys. Rev. B **54**, 11169–11186 (1996).

[35]A. V. Krukau, G. E. Scuseria, J. P. Perdew, and A. Savin, J. Chem. Phys. **129**, 124103 (2008).

[36]K. Momma and F. Izumi, J. Appl. Crystallogr. **44**, 1272–1276 (2011).

[37]A. Kerrigan and K. P. McKenna, GBMaker v1.0.0 (Github, 2022) (2022).

[38]K. P. McKenna and A. L. Shluger, Phys. Rev. B **79**, 224116 (2009).

[39]J. J. Bean, M. Saito, S. Fukami, H. Sato, S. Ikeda, H. Ohno, Y. Ikuhara, and K. P. McKenna, Sci. Rep. **7**, 45594 (2017).

[40]J. A. Quirk, B. Miao, B. Feng, G. Kim, H. Ohta, Y. Ikuhara, and K. P. McKenna, Nano Lett. **21**, 9217–9223 (2021).

[41]S. Petzold, A. Zintler, R. Eilhardt, E. Piros, N. Kaiser, S. U. Sharath, T. Vogel, M. Major, K. P. McKenna, L. Molina-Luna, and L. Alff, Adv. Electron. Mater. **5**, 1900484 (2019).

[42]K. P. McKenna, J. Appl. Phys. **123**, 075301 (2018).

[43]R. E. Williams, Q. M. Ramasse, K. P. McKenna, L. J. Phillips, P. J. Yates, O. S. Hutter, K. Durose, J. D. Major, and B. G. Mendis, ACS Appl. Mater. Interfaces **12**, 21730–21738 (2020).

[44]K. P. McKenna, ACS Energy Lett. **3**, 2663–2668 (2018).

[45]J. Taftø and J. C. H. Spence, J. Appl. Crystallogr. **15**, 60–64 (1982).

[46]J. M. LeBeau, A. J. D'Alfonso, N. J. Wright, L. J. Allen, and S. Stemmer, Appl. Phys. Lett. **98**, 052904 (2011).

[47]K. Tanaka, N. L. Okamoto, S. Fujio, H. Sakamoto, and H. Inui, J. Appl. Crystallogr. **48**, 736–746 (2015).

[48]M. M. Woolfson, *An Introduction to X-ray Crystallography*, 2nd ed. (Cambridge University Press, 1997).

[49]Q. He, C. H. Yeh, J. C. Yang, G. Singh-Bhalla, C. W. Liang, P. W. Chiu, G. Catalan, L. W. Martin, Y. H. Chu, J. F. Scott, and R. Ramesh, Phys. Rev. Lett. **108**, 067203 (2012).

[50]C. Persson and A. Zunger, Phys. Rev. Lett. **91**, 266401 (2003).

[51]M. Frumar, T. Kala, and J. Horák, J. Cryst. Growth **20**, 239–244 (1973).

[52]M. Posfai and M. Sundberg, Am. Mineral. **83**, 365–372 (1998).

[53]D. Hull and D. Bacon, *Introduction to Dislocations*, 1st ed. (Butterworth-Heinemann, Oxford, 2001).

[54]S. H. Yoo, K. T. Butler, A. Soon, A. Abbas, J. M. Walls, and A. Walsh, Appl. Phys. Lett. **105**, 062104 (2014).

[55]A. Abbas, G. D. West, J. W. Bowers, P. Isherwood, P. M. Kaminski, B. Maniscalco, P. Rowley, J. M. Walls, K. Barricklow, W. S. Sampath, and K. L. Barth, IEEE J. Photovoltaics **3**, 1361–1366 (2013).